Vietnam Journal of Earth Sciences, 47(4), 607–634, https://doi.org/10.15625/2615-9783/23783

Vietnam Journal of Earth Sciences
https://vjs.ac.vn/index.php/jse

Assessing WRF-Modeled vertical profiles during MRG wave events on the southern coast of West Java: impact of vertical resolution, domain configuration, and input data

Didi Satiadi[1*], Trismidianto[1], Anis Purwaningsih[1], Wendi Harjupa[1,2,3], Ibnu Fathrio[1], Dita F. Andarini[1], Risyanto[1], Teguh Harjana[1], Alfan S. Praja[1], Noersomadi[1], Fadli Nauval[1], Elfira Saufina[1], Ina Juaeni[1], Adi Witono[1], Aisya Nafiisyanti[1], Eddy Hermawan[1], Robi Muharsyah[4], Danang E. Nuryanto[4], Putri Wulandari[5], Muhaji S. Putri[5]

[1]*National Research and Innovation Agency, Bandung 40135, Indonesia*
[2]*School of Electrical Engineering, Telkom University, Bandung, Indonesia*
[3]*Disaster Prevention Research Institute (DPRI), Kyoto University, Gokasho, Uji, Kyoto 611-0011, Japan*
[4]*The Agency for Meteorology, Climatology and Geophysics, Jakarta, Indonesia*
[5]*Faculty of Earth Sciences and Technology, Bandung Institute of Technology, Bandung, Indonesia*

Received 04 March 2025; Received in revised form 27 September 2025; Accepted 13 November 2025

ABSTRACT

Mixed Rossby-gravity (MRG) waves are key equatorial disturbances that modulate convection and rainfall across the Maritime Continent, yet their representation in regional models remains underexplored. Accurate simulation of MRG waves induced vertical structure is critical for improving forecasts of tropical weather variability and associated hydrometeorological hazards. This study evaluates the Weather Research and Forecasting (WRF) model's ability to simulate vertical atmospheric profiles during an MRG wave event on the southern coast of West Java from 26 to 29 September 2022, using radiosonde observations at 06, 12, and 18 local time (LT). Eleven model configurations were evaluated, differing in domain schemes (two vs. three nesting steps), vertical resolution (33, 45, 60, 80, and 100 levels), and input data sources (Real-Time Global Forecast System [GFS] vs. Final Operational Global Analysis [FNL]). All model configurations used in the simulation have a fixed physics scheme parameterization. The simulations were compared with radiosonde observations and evaluated statistically using the correlation coefficient (R) and Normalized Mean Absolute Error (NMAE). The analysis demonstrates that the WRF model effectively captures MRG wave dynamics by simulating key atmospheric variables, including pressure (P), temperature (T), relative humidity (RH), zonal (U) and meridional (V) wind anomalies in strong agreement with observations. P is well represented, exhibiting the highest R (0.81), whereas RH is the lowest (0.21), likely reflecting the model's inability to capture fine-scale observed moisture variations. Configurations that utilized a two-step nesting domain and the FNL input demonstrated the best performance, achieving higher R values and lower NMAE. Input data had a notable impact on model performance: the FNL analysis improved R by ~36% and reduced NMAE by ~12% compared to GFS, likely due to FNL's assimilation of observational data, which reduces uncertainty. Moreover, a domain scheme with a smaller outer domain and fewer nesting steps also improved R by ~36% and reduced NMAE by ~12%, suggesting that simpler domain configurations help limit error propagation. Additionally, increasing the vertical resolution from 33 to 100 levels enhanced the simulation of MRG wave structures, improving R by ~45% and reducing NMAE by ~22%. These findings enhance the understanding of MRG wave dynamics and offer valuable insights for improving regional weather forecasting.

Keywords: WRF, model assessment, MRG, radiosonde, West Java.

1. Introduction

The Indonesian Maritime Continent (IMC) lies at the heart of the global climate system, exerting a profound influence on regional and global weather patterns (Ramage, 1968; Neale and Slingo, 2003). Embedded within the

*Corresponding author, Email: didi.satiadi@brin.go.id

tropical warm pool, this region experiences a broad spectrum of atmospheric interactions, from diurnal to decadal timescales, that modulate convection, precipitation, and the overall circulation (McBride, 1998; Chang et al., 2004). In particular, the southern coast of West Java, facing the Indian Ocean, is highly vulnerable to these multiscale influences, making it an ideal location for studying land-sea–atmosphere dynamics (Qian et al., 2010) and hydrometeorological hazards such as floods, landslides, and extreme weather events (Marlyono and Nandi, 2018).

A key driver of tropical weather variability in this region is the presence of Convectively Coupled Equatorial Waves (CCEWs). Initially introduced by Matsuno (1966) and further explored by Yanai and Maruyama (1966), CCEWs play a critical role in modulating tropical convection and the Asian monsoon by driving large-scale convective systems. Among these, Mixed Rossby-gravity (MRG) waves, also known as Yanai waves, are equatorially trapped disturbances that combine characteristics of both Rossby and inertio-gravity modes and typically propagate westward with periods of a few days (Kiladis et al., 2009). Their symmetric structure about the equator drives alternating low-level convergence and divergence, initiating convection and modulating tropical rainfall patterns as crests and troughs pass (Wallace, 1971, 1973; Yanai et al., 1968). In the lower troposphere, MRG waves manifest as fluctuations between high-pressure (HP) and low-pressure (LP) phases. At the same time, in the mid-troposphere, they induce shifts in temperature, moisture, and wind anomalies with a pronounced vertical tilt shaped by moist processes that depart from dry-wave theory. Beyond their direct influence on convective heating and momentum transport, MRG waves impact diurnal precipitation cycles and coastal land-sea breeze circulations (Geng et al., 2020). They can even enhance the Madden-Jullian Oscillation (MJO) by driving organized convection, thereby linking regional weather variability to larger-scale climate processes (Takasuka et al., 2019).

Despite substantial advances in our understanding of tropical waves, numerical models still struggle to simulate their complex multiscale interactions over the IMC, essentially because limited spatial resolution hinders representation of diurnal convection and localized land–sea processes (Im and Eltahir, 2018). Various approaches from linear shallow-water formulations (Aiyyer and Molinari, 2003) to regional climate simulations with the National Center for Atmospheric Research's (NCAR) model (Yang et al., 2009), European Centre for Medium-Range Weather Forecasts – Integrated Forecasting System (ECMWF-IFS) analyses (Bengtsson et al., 2019), and the Copernicus Atmosphere Monitoring Service - Coupled System Model (CAMS-CSM) framework (Wang et al., 2019) have sought to capture MRG wave propagation and characteristics. Yet, detailed evaluations against high-resolution in situ observations remain scarce. Likewise, global Numerical Weather Prediction (NWP) systems such as Global Forecast System (GFS) and IFS, while adept at reproducing large-scale tropical variability, tend to underestimate the amplitude and coherence of CCEWs beyond short lead times, with tropical precipitation skill decaying after four days (Bengtsson et al., 2019; Dias et al., 2023). Although the IFS generally outperforms GFS due to more advanced cumulus–Planetary Boundary Layer (PBL) interactions and four-dimensional variational assimilation (Skamarock et al., 2019), even high-resolution global models often simulate waves that propagate too slowly and fail to replicate observed vertical tilt structures (Yang et. al., 2009).

To bridge this gap, the present study evaluates the Weather Research and

Forecasting (WRF) model's ability to simulate vertical profiles during MRG wave events using high-resolution radiosonde observations. Building on earlier research that successfully captured atmospheric dynamics during MRG wave events (Satiadi et al., 2024), this work systematically compares modeled vertical profiles with observations to identify optimal model configurations. By integrating multiple WRF configurations with detailed radiosonde measurements, the study aims not only to pinpoint specific deficiencies in current modeling approaches but also to provide a robust framework for improving operational weather forecasts in regions characterized by complex topography and dynamic atmospheric conditions. While previous research has explored WRF's ability to simulate MRG waves, our study focuses on a case over the southern coast of West Java, a region with limited observational validation. Using local radiosonde data, we aim to assess model performance in this context, which is operationally relevant.

In this context, the WRF model presents several advantages for regional studies of convectively coupled equatorial waves. Its flexible one-way nesting capability allows high-resolution domains to be embedded within coarser grids, enabling the representation of fine-scale topographic and coastal influences, which are essential for accurately simulating MRG wave structures along West Java's southern coast (Skamarock et al., 2008). WRF's advanced physical parameterizations, including boundary-layer, microphysics, and cumulus schemes, support more realistic representations of moist convection and wave-induced vertical motions than many global models. Additionally, its ability to assimilate high-frequency observational data such as radiosondes in real time enhances the model's capacity to capture the evolving background environment and improve short-term wave forecasts (Barker et al., 2012). Furthermore, WRF's open-source architecture and active user community facilitate tailored sensitivity experiments, including variations in vertical resolution and domain configurations, to systematically assess model performance under different scenarios.

In summary, this research offers an innovative approach by combining high-resolution radiosonde data with advanced WRF modeling to assess MRG wave dynamics along the southern coast of West Java. The insights gained from this evaluation are expected to enhance numerical weather prediction and contribute to more effective hydrometeorological risk management across the IMC.

2. Data and Method

2.1. Data

We collected data during a radiosonde campaign at the Pameungpeuk Station (107.7°E, 7.6°S) on the south coast of West Java from 26 to 29 September 2022, at 06, 12, and 18 local time (LT), as shown by the red star in Fig. 1. Radiosondes provide detailed vertical profiles of key atmospheric parameters; in this study, we used Vaisala radiosondes (Vaisala, n.d.) to measure pressure (P), temperature (T), relative humidity (RH), zonal wind (U), and meridional wind (V).

Given the region's sparse observational network, this campaign offers a valuable opportunity to evaluate the WRF model's ability to simulate atmospheric phenomena, such as MRG wave propagation. Although we focus on a single event, our findings provide important insights into model performance and serve as a benchmark for future studies. A broader evaluation involving multiple cases across various periods and conditions is needed to fully assess the robustness of the model configurations and sensitivities presented here.

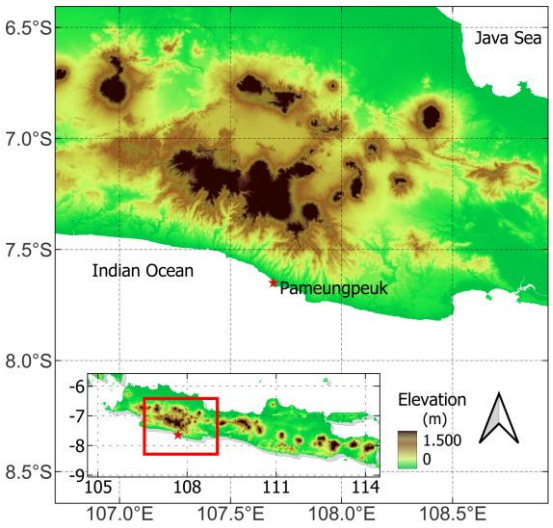

Figure 1. Map of the study area. The Red Star symbol indicates the location of the Pameungpeuk Station (107.7°E, 7.6°S) on the southern coast. of West Java

Previous studies have shown that MRG waves are most pronounced during the boreal summer and fall (Liebmann and Hendon, 1990; Magana and Yanai, 1995; Roundy and Frank, 2004), particularly from July to October. Recent work further indicates that the complex environment of the Maritime Continent can support localized MRG wave activity, despite earlier findings of strong signals over the North Pacific (Kiladis et al., 2009; Wang et al., 2019). Our study (Satiadi et al., 2024) identified MRG waves off southern West Java, with targeted radiosonde observations providing valuable data for model validation.

To further identify MRG wave events, we used Outgoing Longwave Radiation (OLR) data from the National Oceanic and Atmospheric Administration (NOAA's) Climate Data Record (CDR) version 1.2 (Lee, 2011) for the period 2000-2004, available at https://www.ncei.noaa.gov/data/outgoing-longwave-radiation-daily/access/.

In addition to observational data, we employed outputs from WRF model simulations using eleven (11) different configurations to assess their ability to capture the propagation of MRG waves during the same period (26-29 September 2022). The WRF model is a widely used open-source community tool for research and operational numerical weather prediction (Skamarock et al., 2021). In our study, WRF outputs include vertical profiles of P, T, RH, U, and V, allowing for direct comparison with the radiosonde observations.

2.2. Methods

We identified MRG wave events by analyzing daily OLR anomalies from 26 to 29 September 2022. The anomalies were calculated by subtracting the 25-year daily climatology (1 January 2000–31 December 2024) from the corresponding daily OLR values. We also removed the first three harmonics from the dataset to eliminate low-frequency components. To isolate MRG wave signals, we applied a bandpass filter to the daily OLR anomalies for the period 3 March 2022 to 31 March 2023. In this case, zero padding was not used because the filtered data span significantly exceeds the study period. The filter targeted zonal wavenumbers 1–10, periods of 3–10 days, and equivalent depths of 8–90 m, following the methodologies of Wheeler and Weickmann (2001) and Schreck et al. (2011).

We then simulated the Southern Coast of West Java using the WRF model, a widely recognized tool for both research and operational weather prediction due to its ability to simulate atmospheric processes across multiple scales (Skamarock et al., 2021). The WRF model was chosen for its proven capability to resolve tropical atmospheric dynamics, including the propagation of MRG waves, and for its flexibility in configuration and parameterization, which is critical for addressing the regional complexities of West Java.

To evaluate model performance, we employed 11 different configurations denoted A1, A2, A3, A4, A5, A6, A7, B1, B2, B3, and B4 (see Table 1) to systematically examine the effects of domain schemes, vertical resolution, and model input data.

Table 1. WRF Model Configurations

Domain	**A**							**B**			
1st nesting	D1: 175 × 201 grids, 5 km res.							D1: 599 × 599 grids, 9 km res.			
2nd nesting	D2: 401 × 401 grids, 1 km res.							D2: 588 × 588 grids, 3 km res.			
3rd nesting	-							D3: 570 × 567 grids, 1 km res.			
Configuration	**A1**	**A2**	**A3**	**A4**	***A5***	***A6***	***A7***	**B1**	**B2**	**B3**	**B4**
Grid Size	401 × 401							570 × 567			
Spatial Resolution	1 km							1 km			
Input	FNL	GFS	FNL	GFS	*FNL*	*FNL*	*FNL*	FNL	GFS	FNL	GFS
Vertical Levels	33	33	45	45	*60*	*80*	*100*	33	33	45	45
Physical Scheme	**A1**	**A2**	**A3**	**A4**	***A5***	***A6***	***A7***	**B1**	**B2**	**B3**	**B4**
Cumulus	Betts Miller Janjic/BMJ										
Microphysics	WSM-3 Class										
Long Wave Radiation	RRTM/Dhudia										
Shortwave Radiation	RRTM/Dhudia										
Boundary Layer	Yonsei University										
Surface Layer	Revised MM5 Monin-Obukov										
Land Surface	NOAH										

In domain scheme A (applied in configurations A1, A2, A3, A4, A5, A6, and A7), a two-step nesting process was used: the simulation transitioned from domain D1 (175×201 grid points) at a 5 km resolution to domain D2 (401×401 grid points) at a 1 km resolution. This scheme is identical to that used in our routine prediction experiments at our research center (Prihanto et al., 2023). In contrast, domain scheme B (applied in configurations B1, B2, B3, B4) utilized a three-step nesting process: starting with domain D1 (599×599 grid points) at a 9 km resolution, refining to domain D2 (588×588 grid points) at a 3 km resolution, and finally to domain D3 (570×567 grid points) at a 1 km resolution. This approach allowed us to investigate whether the more complex three-step nesting with a broader outer domain would better capture MRG waves and their interactions with larger-scale atmospheric forcing (Fig. 2).

A horizontal resolution of 1 km is generally sufficient to capture the key features of the vertical profile variability observed at a radiosonde location, particularly when paired with high vertical resolution and carefully selected physical parameterizations. Radiosondes provide excellent vertical detail, but previous studies have demonstrated that high-resolution numerical models such as WRF, when configured appropriately, can reproduce the main vertical structures of temperature, humidity, and wind profiles with reasonable accuracy. For example, Coniglio et al. (2013) found good agreement between WRF simulations and radiosonde observations for thermodynamic and kinematic structures during convective events. Similarly, Feng et al. (2018) showed that WRF at convection-permitting scales (<4 km) captures key vertical features of mesoscale convective systems. While some small-scale variability may still be smoothed by vertical discretization, the essential characteristics of vertical profiles can be effectively represented at 1 km resolution for most mesoscale applications.

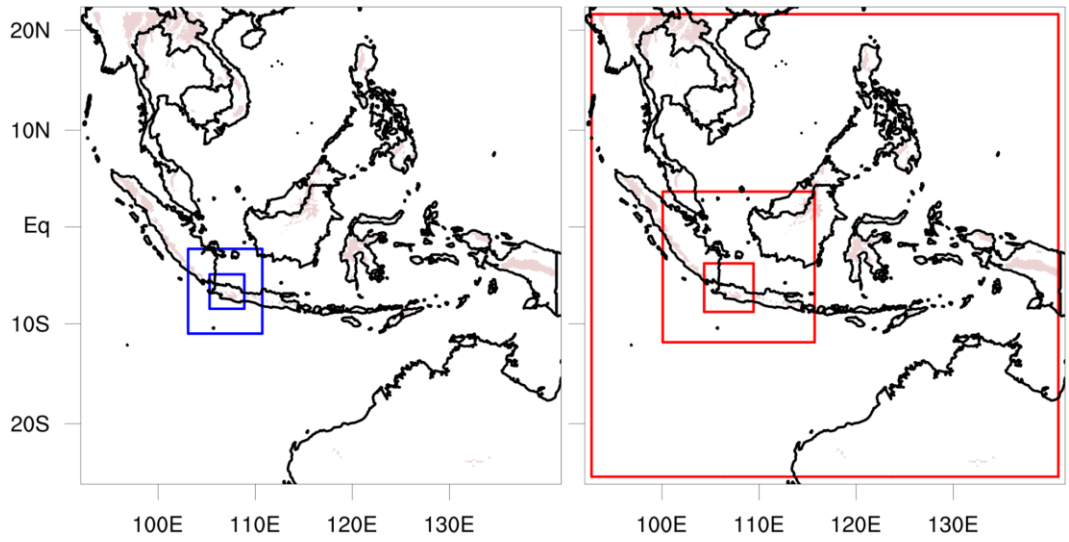

Figure 2. The domain scheme A (blue squares, 2-step nesting) and B (red squares, 3-step nesting)

Moreover, while a 1 km horizontal resolution does not resolve microscale variability, it is generally sufficient to capture mesoscale vertical structures relevant to tropical wave processes. Prior studies have used similar or coarser resolutions to evaluate model performance against radiosonde observations in tropical regions with meaningful results (Ramos-Valle et al., 2013). At 1 km, the WRF model also improves representation of convection, wave-induced vertical motion, and orographic effects (Skamarock et al., 2008), making it suitable for studying vertical profile variability associated with MRG wave events.

Configurations A1, A2, B1, and B2 used 33 vertical levels to match the 34-level vertical structure of the input data. Configurations A3, A4, B3, and B4 employed 45 vertical levels to assess the impact of slightly enhanced vertical resolution. To further examine the effect of higher vertical resolution, configurations A5, A6, and A7 were implemented with 60, 80, and 100 vertical levels, respectively, using only FNL input. This choice was based on previous experiments, which showed that FNL input combined with a simpler two-nesting domain generally yields better results. We anticipated that the higher vertical resolution would better represent the atmospheric structure, thereby enhancing the simulation of MRG wave characteristics. This comparison reflects our hypothesis that increased vertical resolution improves the model's sensitivity to small-scale vertical processes (e.g., atmospheric turbulence) and the propagation of MRG waves. In all simulations, the model top was set to 50 hPa without Rayleigh upper-level damping.

We also assessed the impact of different model inputs. Configurations A1, A3, A5, A6, A7, B1, and B3 used the National Centers for Environmental Prediction (NCEP)-FNL post-processed reanalysis products that incorporate a wealth of observational data. In contrast, configurations A2, A4, B2, and B4 used the NCEP-GFS, which provides real-time forecast data. This comparison was crucial for determining whether real-time forecast inputs versus post-processed analysis significantly affect the model's ability to simulate MRG waves. We expected that FNL data, owing to its assimilation of observations, might better capture the synoptic-scale conditions influencing MRG wave propagation.

While the superior performance of FNL over GFS is well-established, we aim to quantify this difference specifically in the context of MRG wave simulation and highlight its practical significance, given that GFS is often the only available input for real-time forecasting in many operational settings. This is important because operational forecasts usually rely solely on GFS, and understanding its limitations helps assess the impact of input data quality on model performance in data-sparse regions such as the Maritime Continent.

The physical parameterization schemes used in the simulations are also summarized in Table 1. The choice of schemes in this study was primarily based on previous studies that demonstrated their effectiveness in simulating convective systems and tropical atmospheric processes relevant to our study region. These include the Betts-Miller-Janjic (BMJ) cumulus parameterization, which has been shown to improve precipitation forecasts in the tropical areas (Argüeso et al., 2020; Fonseca et al., 2015). Note that the BMJ scheme was applied only in the larger domain, where convection cannot be resolved explicitly; in the smallest domain, convection was calculated explicitly, eliminating the need for cumulus parameterization. We also employed the WRF Single-Moment 3-Class (WSM-3) microphysics scheme, which is effective at capturing convective systems in tropical environments (Hong and Lim, 2006). To represent radiative processes critical for cloud formation and atmospheric wave dynamics in the tropics, the Rapid Radiative Transfer Model (RRTM) was used for both longwave and shortwave radiation (Xalxo et al., 2022). For turbulent mixing and vertical transport within the boundary layer in tropical environments, the Yonsei University planetary boundary layer scheme was selected (Hernández et al., 2024). Additionally, the revised Fifth-Generation NCAR Mesoscale Model (MM5), the Monin-Obukhov surface layer scheme, and the NOAH land surface model (developed by NCEP, Oregon State University, the Air Force, and the Hydrologic Research Lab.) were incorporated to accurately simulate land-sea interactions essential for coastal regions like West Java (Giannaros et al., 2019).

All simulations were conducted over the West Java region for six days from 25 to 30 September 2022. Each simulation was initialized on 25 September 2022 (00 UTC), allowing a one-day spin-up period, which is generally sufficient for model adjustment in WRF (Skamarock et al., 2008). The model output included hourly vertical profiles of P, T, RH, U, and V from 26 to 29 September 2022.

To evaluate the model's performance, we extracted data from the WRF model grid point closest to the radiosonde launch site (107.7°E, 7.6°S). We averaged the vertical profiles over a 3×3 grid box (nine grid points) centered at that location. The averaged profiles were then interpolated to uniform vertical levels at 50-meter intervals using the piecewise cubic Hermite interpolating polynomial (PCHIP) method (Fritsch and Carlson, 1980), which preserves the shape and monotonicity of the original data. Since our focus is on wave-induced fluctuations rather than general model bias, we constructed both simulated and observed anomalies by subtracting their respective mean profiles over the same analysis period. For each model configuration, we computed profile anomalies by subtracting the mean simulated profile. We compared them with radiosonde anomalies obtained by interpolating the observed profiles to the same vertical levels and subtracting the mean radiosonde profile for the 26–29 September 2022 period. A moving average with a window size of 5 was also applied to the radiosonde anomaly profiles to smooth high-frequency fluctuations while preserving the overall profile shape.

Our analysis of vertical profile anomalies for these variables is based on fundamental wave dynamics. According to linear wave theory, each variable oscillates in both time and space, with its amplitude and phase capturing the wave's propagation characteristics (e.g., Holton and Hakim, 2012; Andrews et al., 1987). By examining these anomalies, we captured the wave's vertical distribution and oscillatory nature at each spatial point. Presenting all five variables not only illustrates their independent oscillatory behavior but also reveals their interrelationships, providing a comprehensive depiction of MRG wave dynamics. For example, the coupling between wind components and temperature perturbations is a key indicator of convectively coupled equatorial waves (Wheeler and Kiladis, 1999). Although our figures focus on the vertical structure at specific locations, together they provide robust evidence of the simulated MRG wave behavior and capture the spatial evolution and interactions of the wave's key features.

To assess the model's ability to capture MRG wave propagation, we compared the simulated anomalies with radiosonde observations. These observations were collected during a period coinciding with the propagation of an MRG wave, specifically during the transition from an HP to an LP system. They were taken from the southern portion of the theoretical MRG wave structure (see Fig. 3c in Kiladis et al., 2009). This comparison enabled us to evaluate how well the simulations replicated the key atmospheric dynamics associated with MRG wave activity during the study period.

Finally, to evaluate the model's accuracy in simulating the observed data, we employed two metrics: the Correlation Coefficient (R) and the Normalized Mean Absolute Error (NMAE). The R quantifies the strength and direction of the linear relationship between model outputs and observations, providing insight into how well the model captures the overall trend of the data. In contrast, the NMAE provides a scale-independent measure of the absolute difference between model predictions and observations, enabling consistent error comparison across variables with different units and scales.

The R is calculated as follows (Koh et al., 2012):

$$R = \frac{\Sigma(X_i - \bar{X})(Y_i - \bar{Y})}{\sqrt{\Sigma(X_i - \bar{X})^2 \ \Sigma(Y_i - \bar{Y})^2}} \quad (1)$$

X and Y represent the model and observed values, $\bar{X}$ and $\bar{Y}$ denote their means. This metric ranges from -1 to 1, with values closer to 1 indicating a strong positive correlation.

The NMAE is defined as (Yu et al., 2006):

$$NMAE = \frac{\Sigma|X_i - Y_i|}{\Sigma(Y_i)} \quad (2)$$

Together, these metrics provide a balanced and comprehensive assessment of the model's performance in simulating MRG wave dynamics.

3. Results and Discussions

3.1. Identification of MRG waves

The MRG wave event was identified by analyzing OLR anomalies from 26 to 29 September 2022 relative to the 25-year mean (2000–2024) that were filtered for zonal wavenumbers 1–10, periods of 3–10 days, and equivalent depths of 8–90 m, following the methodologies of Wheeler and Weickmann (2001) and Schreck et al. (2011). As shown in Fig. 3, the resulting OLR anomaly fields from 24 September to 1 October 2022 depict a coherent westward-propagating MRG wave across the Maritime Continent.

At Pameungpeuk Station on the southern coast of West Java, the wave's passage is evident in the alternation between positive (suppressed convection) and negative (enhanced convection) OLR anomalies. Specifically, the station experiences a dry phase (positive anomalies) on 26–27

September 2022, followed by a transition to a wet phase (negative anomalies) on 28–29 September 2022. This timing coincides with the wave crest and trough passing over the region, underscoring how the MRG wave modulated local convective activity during the radiosonde observation period. The spatial and temporal pattern of OLR anomalies is consistent with the typical characteristics of MRG waves, namely, their westward group velocity and relatively short period, demonstrating the wave's role in influencing weather patterns along the southern coast of West Java.

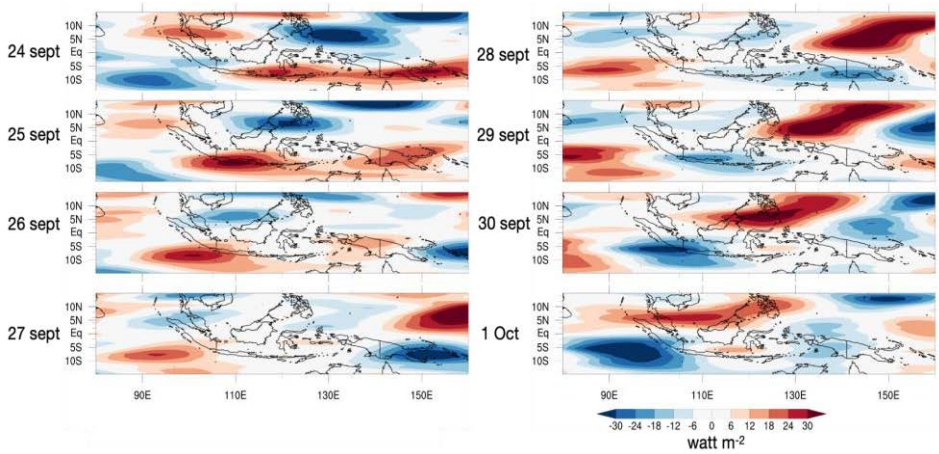

Figure 3. Propagation of the MRG wave based on OLR anomalies from 24 September to 1 October 2022

These findings align with Satiadi et al. (2024), who used Hovmöller analyses of vertically integrated water vapor from Global Navigation Satellite System - Radio Occultation (GNSS-RO) data to highlight the MRG wave's distinct periodicity and distinguish it from other equatorial waves. Additional confirmation was achieved using the fifth-generation ECMWF global reanalysis (ERA5) data, where time-space spectral and wavelet analyses revealed key features of MRG wave propagation (Satiadi et al., 2024). Furthermore, time-series analyses confirmed the MRG wave's substantial contribution compared to other equatorial waves and larger-scale circulation systems.

Figure 4 presents a subset of WRF simulation results (Configuration A1 and A7) and radiosonde observations that capture an MRG wave event over the study area near Pameungpeuk Station. Configurations A1 and A7 use 2-step nesting with FNL input, employing 33 and 100 vertical levels, respectively. Although the analysis focuses on a segment of the wave rather than its entire wavelength, the time-height cross-sections of P, T, RH, U and V anomalies from the model output (Fig. 4f-j and 4k-o) calculated relative to the mean profile over the period of 26 to 29 September 2022 closely matches the corresponding radiosonde data (Fig. 4a-e). The simulation successfully captures key features during the transition from a dry to a wet phase, including a decrease in lower-tropospheric P anomalies, an increase in mid-tropospheric T, decreases and increases in RH, and a weakening of U and V as the wet phase is approached.

Specifically, the WRF simulation shows a steady decline in P anomalies from 26 to 29 September 2022, most notably in the lower atmosphere (Fig. 4f and 4k). This decrease, a hallmark of MRG wave propagation, reflects the transition from HP to LP regions and is typically accompanied by upward motion that enhances moisture convergence and convection (Kiladis et al., 2009; Wheeler and Kiladis, 1999).

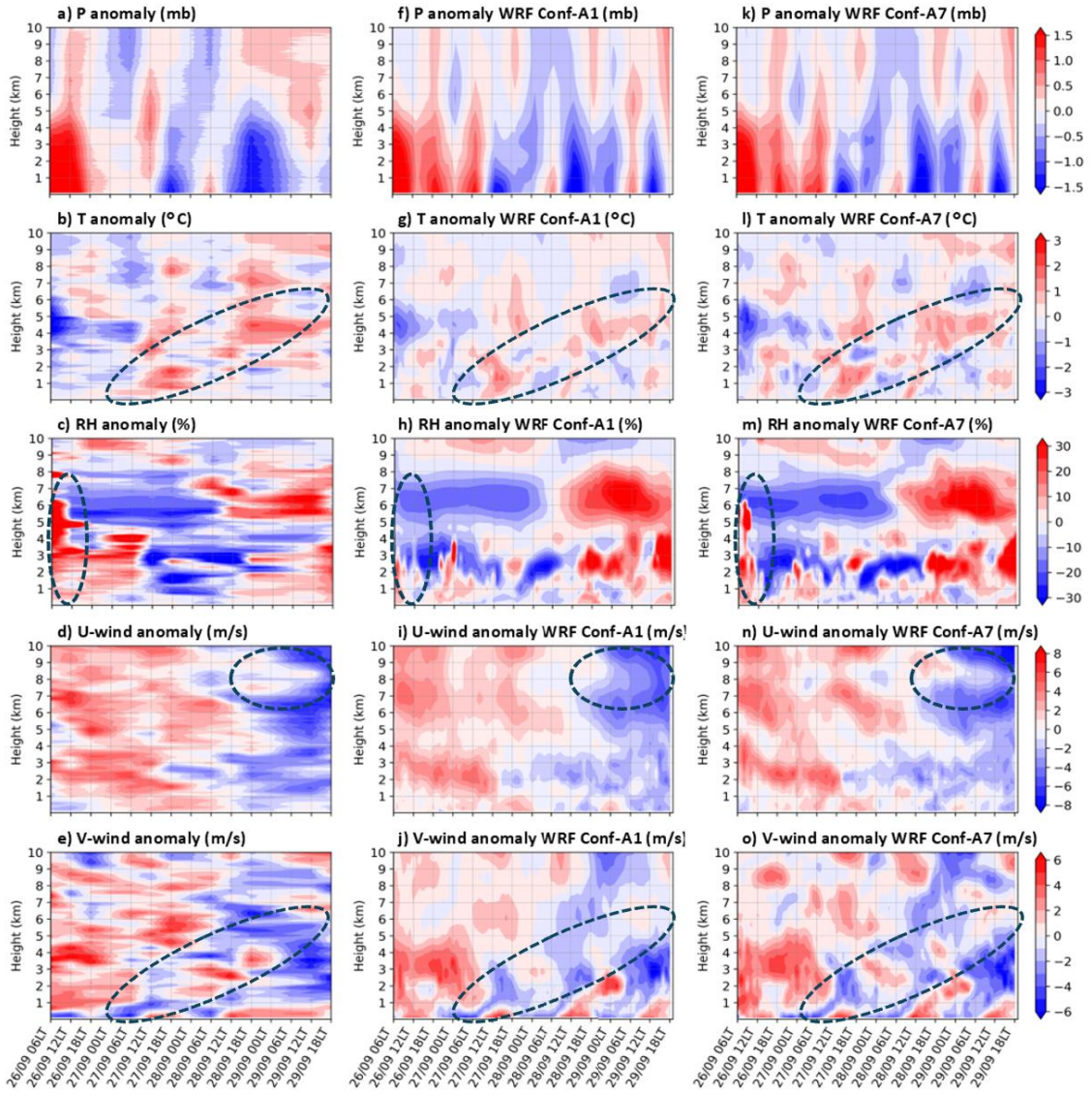

Figure 4. Time-height cross-section of P, T, RH, U, and V anomalies during the MRG wave event from radiosonde observations (a-e) and WRF simulation results for configuration A1 (f-j) and A7 (k-o)

Figures 4g and 4l show an increase in mid-tropospheric T anomalies, likely due to latent heat release during condensation. As the wave moves from HP to LP regions, the updrafts trigger convection: rising air cools, reaches saturation, and condenses, releasing latent heat that warms the surrounding air. This process is consistent with convection-driven temperature increases observed during MRG wave events (Kiladis et al., 2009). Furthermore, the vertical tilt in the T anomalies is visible in Fig. 4g and 4l. Wheeler et al. (2000) suggested that these vertical structures are linked to vertically propagating short-wavelength signals in the troposphere, which play a crucial role in coupling large-scale dynamics with convection.

The increase in RH depicted in Figures 4h and 4m further supports this mechanism. Upward motion transports moisture to higher

altitudes, leading to cooling and saturation, which promotes cloud formation and precipitation. This enhanced moisture convergence, particularly in the lower and mid-troposphere, reinforces the convective processes characteristic of MRG waves (Wheeler et al., 2000; Straub and Kiladis, 2003).

Figures 4i-j and 4n-o illustrate a consistent decline in both U and V anomalies. The reduction in U aligns with theoretical expectations of a decelerating eastward flow during the HP-to-LP transition (Holton and Hakim, 2012), while the weakening of V indicates a diminished north-south flow. Moreover, the observed vertical tilt in V anomalies supports previous findings from radiosonde data at Majuro Island (7.1°N, 171.4°E) in the Central Pacific (Kiladis et al., 2009).

Collectively, these results demonstrate that the model, using both 33 and 100 vertical levels, accurately reproduces the key features of MRG wave propagation. The patterns observed in P, T, RH, U, and V align with the expected atmospheric transition from HP to LP systems under the influence of MRG waves, consistent with the theoretical framework outlined by Kiladis et al. (2016).

Overall, both Configurations A1 (33 levels) and A7 (100 levels) capture the broad height-time patterns seen in the radiosonde data, but A7 consistently provides a closer match to the fine-scale structure. First, A7 reproduces the amplitude of the anomalies more faithfully: its stronger positive and negative excursions in pressure and temperature more closely bracket the observed extremes. In particular, the slanted "tilt" of the temperature anomalies from mid to upper levels which in the radiosonde appears as an upward-propagating warming signal is better defined in A7 (cf. panels b, l, and g) than in A1 (panel g). Second, A7 also more accurately captures the vertical extent of the moisture anomalies on 26 September: the observed deep moist layer from about 2–6 km is reproduced in A7 (panel m) but underrepresented in A1 (panel h). Third, at upper levels on 29 September, the westerly wind anomaly peak (around 8–10 km) and its timing align more closely with the observation in A7 (panel n) than in A1 (panel i). Finally, the meridional wind tilt evident as a downward-sloping southerly anomaly between 2 and 6 km emerges more cleanly in A7 (panel o) than in A1 (panel j). In sum, while both configurations capture the first-order features, the higher vertical resolution of A7 enables it to resolve the vertical structure and amplitude of the radiosonde anomalies with greater fidelity.

3.2. Assessment of WRF-Modeled Vertical Profiles

Figure 5 presents vertical profiles of P anomalies derived from radiosonde observations (black lines) and from WRF simulations using 11 different configurations (colored lines) for 26–29 September 2022 at 06, 12, and 18 LT. The values at the bottom of each panel represent the column and daily averages of the observed anomalies. Blue text indicates positive anomalies, while red indicates negative anomalies. These values provide a quick overview of the anomaly trends as the wave progresses.

These profiles highlight a clear transition in the lower troposphere (0–5 km), where P anomalies shift from positive to negative over the study period. This transition reflects the propagation of the MRG wave from HP to LP systems, leading to a decrease in P at the location, consistent with the MRG wave's horizontal structure described by Kiladis et al. (2009).

Overall, the vertical profiles from the simulations generally match the observed trends, though some discrepancies emerge, particularly in the lower troposphere at

midday. These differences likely reflect differences in model configurations and enhanced surface dynamics in the afternoon (Holton and Hakim, 2012). The differences between nighttime and daytime biases may also stem from radiation-related errors during daytime (Luers, 1997; Vömel et al., 2007; Nash et al., 2010). Specifically, solar radiation can affect the temperature and humidity sensors of radiosondes, leading to discrepancies in measurements compared to nighttime observations, when such radiation is absent (Lanzate and Free, 2008; Minnis et al., 2005).

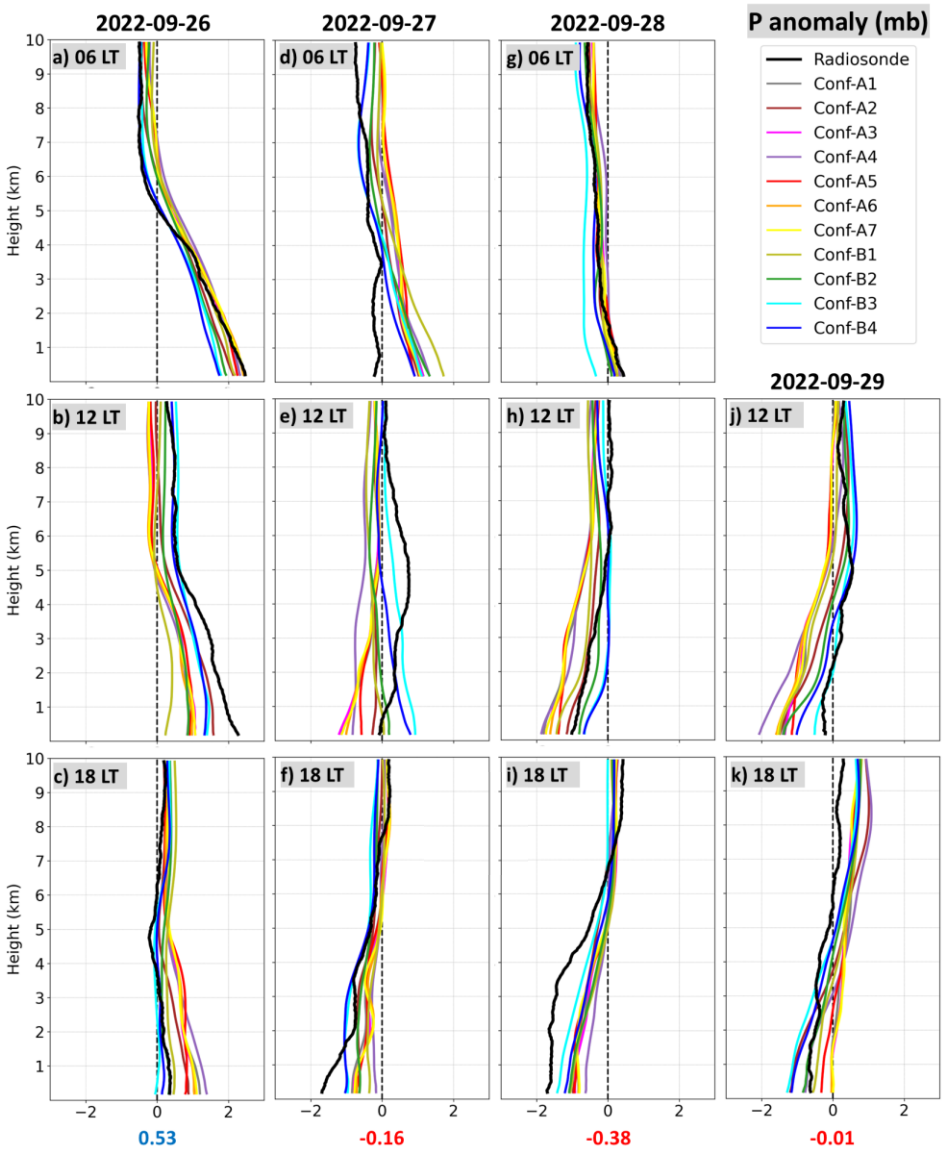

Figure 5. Vertical profiles of P anomalies during 26-29 September 2022 at 06, 12, and 18 LT: Comparison between radiosonde observation (black line) and WRF simulation with 11 distinct configurations (colored lines). The values at the bottom of each panel represent the column and daily averages of the observed anomalies

Most of the P fluctuations occur below 5 km, indicating that the MRG wave exerts its most decisive influence in the lower troposphere. In contrast, upper- tropospheric fluctuations are comparatively muted, suggesting the wave's primary impact remains confined to lower atmospheric levels. The results are consistent with Takayabu (1994), who suggested that the adequate level lies in the lower troposphere, where moisture content and disturbance amplitudes are high. Similarly, Kiladis et al. (2009) stated that MRG waves, when coupled with convection, exhibit shallower equivalent depths and produce significant perturbations in the lower troposphere.

Despite these variations, all simulations capture the transition from positive to negative P anomalies, demonstrating the WRF model's capability to depict MRG wave propagation at this location. The results align with the theoretical MRG structure proposed by Kiladis et al. (2016) and corroborate previous findings by Satiadi et al. (2024).

Figure 6 illustrates the evolution of T anomalies from 26 to 29 September 2022, highlighting a transition from negative to positive values, particularly in the mid-troposphere. This transition confirms the notable influence of MRG waves on tropical T anomalies, as documented by Holton and Hakim (2012) and Fathullah et al. (2017).

The vertical profiles of T anomalies derived from WRF simulations (colored lines) generally match the observed patterns (black lines), although notable differences emerge among model configurations. In particular, simulated T anomalies show a larger bias relative to observations than simulated P anomalies, reflecting the inherent challenges of accurately modeling temperature-related processes. Moreover, observed temperature anomalies exhibit greater variability than their simulated counterparts, likely due to the model's coarser vertical resolution, which tends to smooth out the finer- scale fluctuations captured by radiosonde data.

A closer examination of the vertical structure reveals that T anomalies are most pronounced in the mid-troposphere, where convection and cloud formation are most active. This finding aligns with Kiladis et al. (2009), who suggested that the primary energy source for MRG waves is diabatic heating from moist convection in the troposphere. During this period, enhanced convection associated with the MRG wave's passage may drive more substantial variability. The upward transport of moisture, followed by condensation and latent heat release, appears to be responsible for the shift from negative to positive temperature anomalies (Kiladis et al., 2009). This shift also suggests a progression from subsidence-induced cooling to warming driven by convective processes, underscoring the wave's dynamic impact on local atmospheric stability.

Although the simulations capture the broad transition from negative to positive T anomalies, the agreement between observed and simulated profiles is closer on 26 September 2022 than during the subsequent days (27–29 September). This increasing discrepancy may indicate that the MRG wave dynamics are becoming more complex over time, potentially interacting with other atmospheric waves or systems in ways the model struggles to resolve fully. Such complexities likely highlight the limitations of current physics parameterizations.

Despite these challenges, the simulations successfully reproduce the overall shift in T anomalies, underscoring the WRF model's capacity to represent the influence of MRG wave propagation on T structure. These findings align with the anticipated increase in latent heat release and consequent warming, which follows the MRG wave's progression from HP to LP regions, as described by Kiladis et al. (2009).

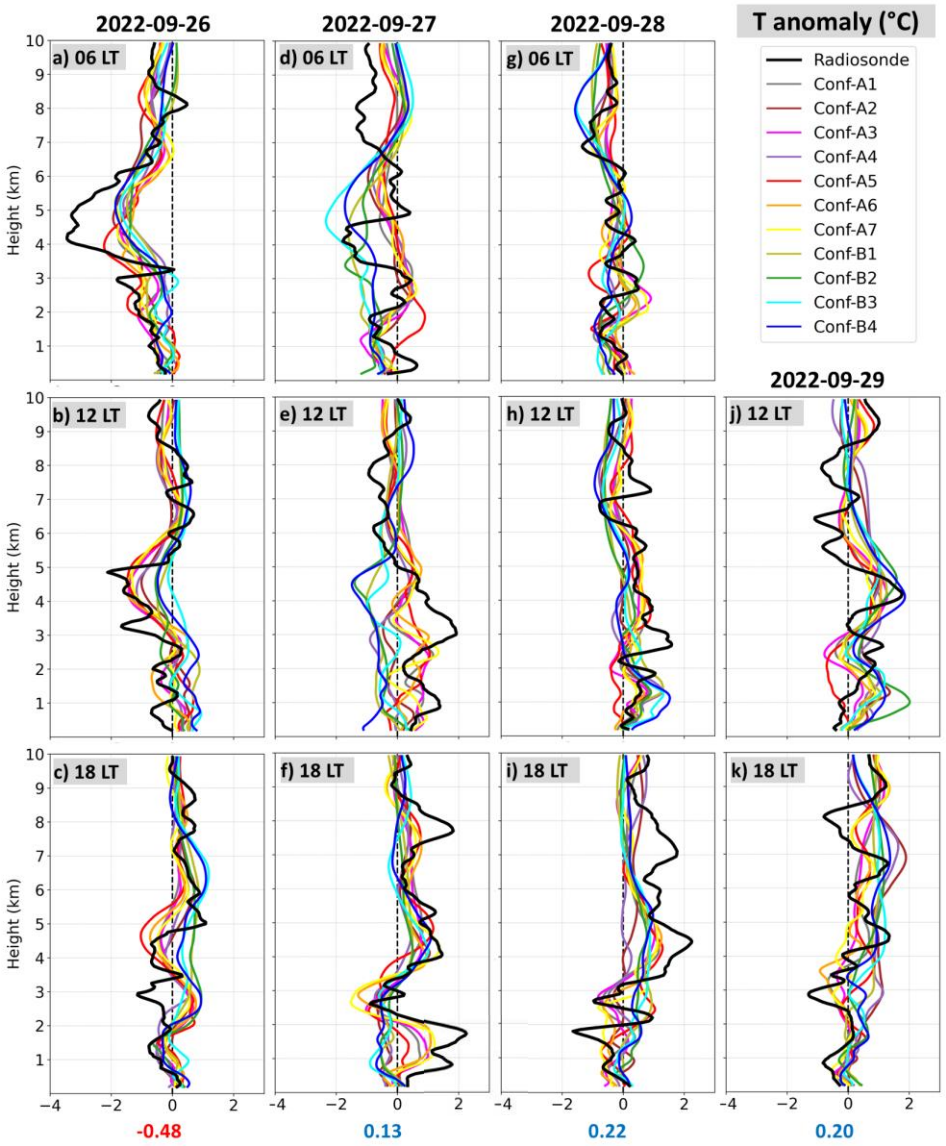

Figure 6. As in Fig.5, but for T

Figure 7 presents observed and simulated vertical profiles of RH anomalies from 26 to 29 September 2022, highlighting a transition from positive to negative and then back to positive values. This pattern aligns with the MRG wave's progression from HP to LP systems (Kiladis et al., 2009), reflecting the wave's passage through dry and wet phases and its influence on local moisture content (Holton and Hakim, 2012).

When examined alongside the P and T analyses, these RH anomalies reveal the dynamic interactions governing MRG wave propagation. Between 26 and 27 September, the shift from positive to negative RH anomalies corresponds to the wave's dry phase, typically characterized by subsidence. By 28–29 September, the re-emergence of positive RH anomalies signals a transition to the wet phase, commonly featuring enhanced upward motion, lower P, and increased convection. This convective activity transports

moisture into the mid and upper troposphere, creating a moist environment that typifies MRG wave effects (Kiladis et al., 2009).

Although the simulated RH profiles generally follow the observed trends, biases appear on 26 and 27 September 2022. On 26 September, the model underestimated RH, possibly because it overestimated subsidence. Conversely, on 27 September, it overestimates RH, which may stem from premature or exaggerated upward motion that intensifies moisture convergence. These discrepancies likely reflect the challenges of accurately capturing the timing and strength of the MRG wave's impact on convection and moisture transport.

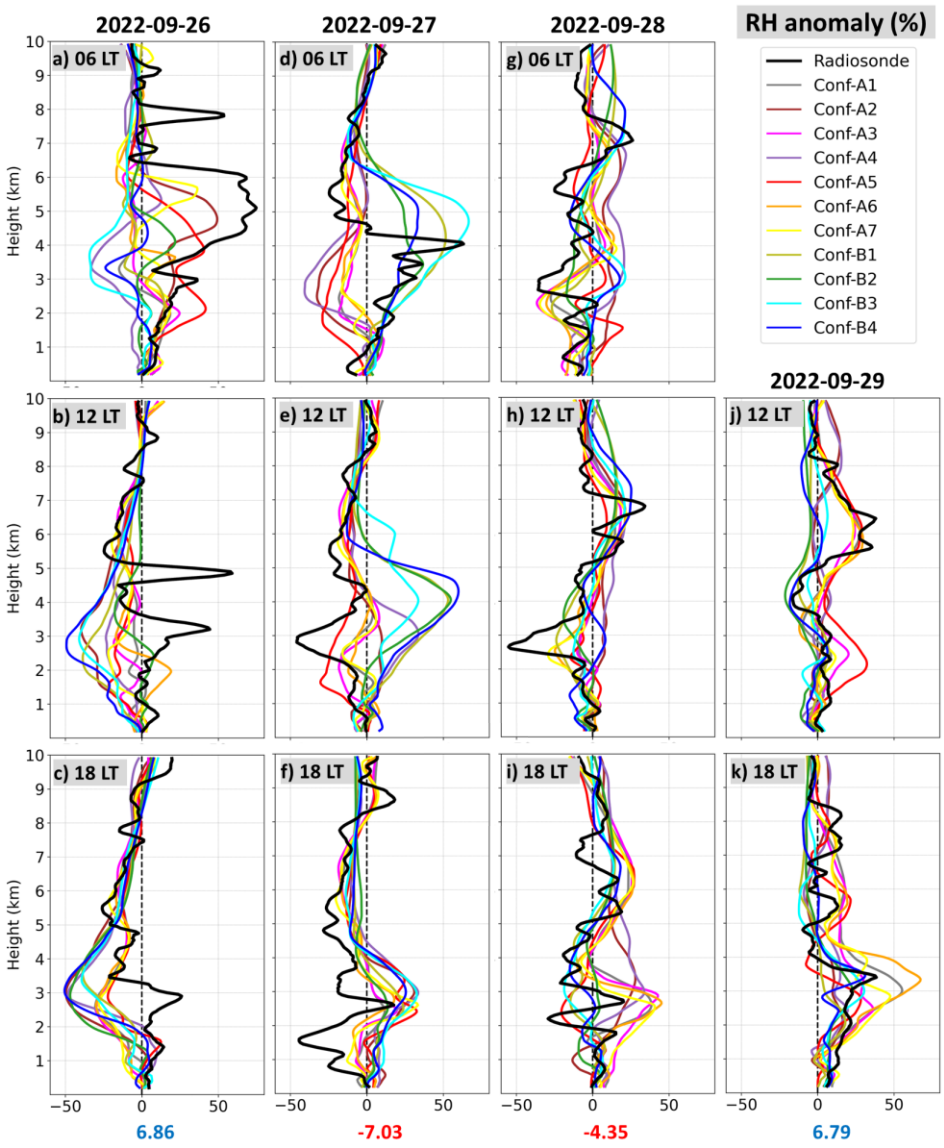

Figure 7. As in Fig.5, but for RH

The magnitude of discrepancies in RH between radiosondes and models can vary depending on atmospheric conditions, such as temperature, humidity, and stability.

Radiosondes provide high vertical-resolution measurements, whereas models may have coarser vertical levels, leading to differences in RH profiles. Models may not capture the fine-scale variations in RH that radiosondes can measure, especially in complex atmospheric conditions. Models also rely on parameterizations of processes such as cloud formation and precipitation, which can affect RH calculations and contribute to discrepancies.

Despite these limitations, the simulations successfully reproduce the overall evolution of RH anomalies, including the return to positive values linked to the wave's wet phase. This outcome underscores the MRG wave's significant role in modulating tropospheric moisture and demonstrates the model's ability to depict the broader wave progression. The interplay among P, T, and RH during this period underscores the MRG wave's role in shaping local atmospheric dynamics, with RH anomalies closely tied to the wave's structure and its influence on convective processes (Kiladis et al., 2009).

Figure 8 illustrates a pronounced transition in U anomalies from predominantly positive to negative between 26 and 29 September 2022, as observed in the radiosonde data (black lines). This shift from positive to negative wind anomalies strongly reflects the influence of the MRG wave, consistent with its characteristic progression from HP to LP systems (Kiladis et al., 2009; Holton and Hakim, 2012). Notably, the marked negative anomalies on 29 September indicate the arrival of the wave's wet phase, corresponding to the LP system.

This transition underscores the dynamic forcing exerted by the MRG wave, which significantly affects the wind field in the lower and mid-troposphere. As the wave propagates, it generates alternating zones of convergence and divergence, leading to fluctuations in wind direction (Kiladis et al., 2009). The observed shift in wind anomalies captures this wave-induced alternation, with the wet phase indicating enhanced convergence that likely intensifies convective activity, as evidenced by the temperature and humidity analyses.

The simulated U wind anomalies (colored lines) generally replicate the observed patterns, capturing the overall impact of the MRG wave on the wind field. However, the simulations display lower variability than the radiosonde data, suggesting that model resolution or physics parameterizations may smooth out some of the finer-scale wave-induced fluctuations. Additional factors, such as local topography and smaller-scale atmospheric disturbances, may further contribute to discrepancies between the model and observations (Holton and Hakim, 2012). Nevertheless, the WRF model's ability to reproduce the transition from positive to negative U anomalies demonstrates its effectiveness in depicting the MRG wave's influence on the wind field (Kiladis et al., 2009).

This shift in U anomalies also aligns with the findings from the P, T, and RH analyses. As the MRG wave advances from HP to LP systems, it not only modifies T and RH but also significantly affects the U wind component (Kiladis et al., 2009). The negative anomalies associated with U likely indicate enhanced convergence at the wave trough, fostering upward motion and convective activity, as observed in the T and RH profiles. These interconnected changes in U, V, P, T, and RH anomalies collectively illustrate the wave's dynamic influence on the atmosphere, serving as a key indicator of the MRG wave's passage and broader effects on the tropical troposphere (Holton and Hakim, 2012).

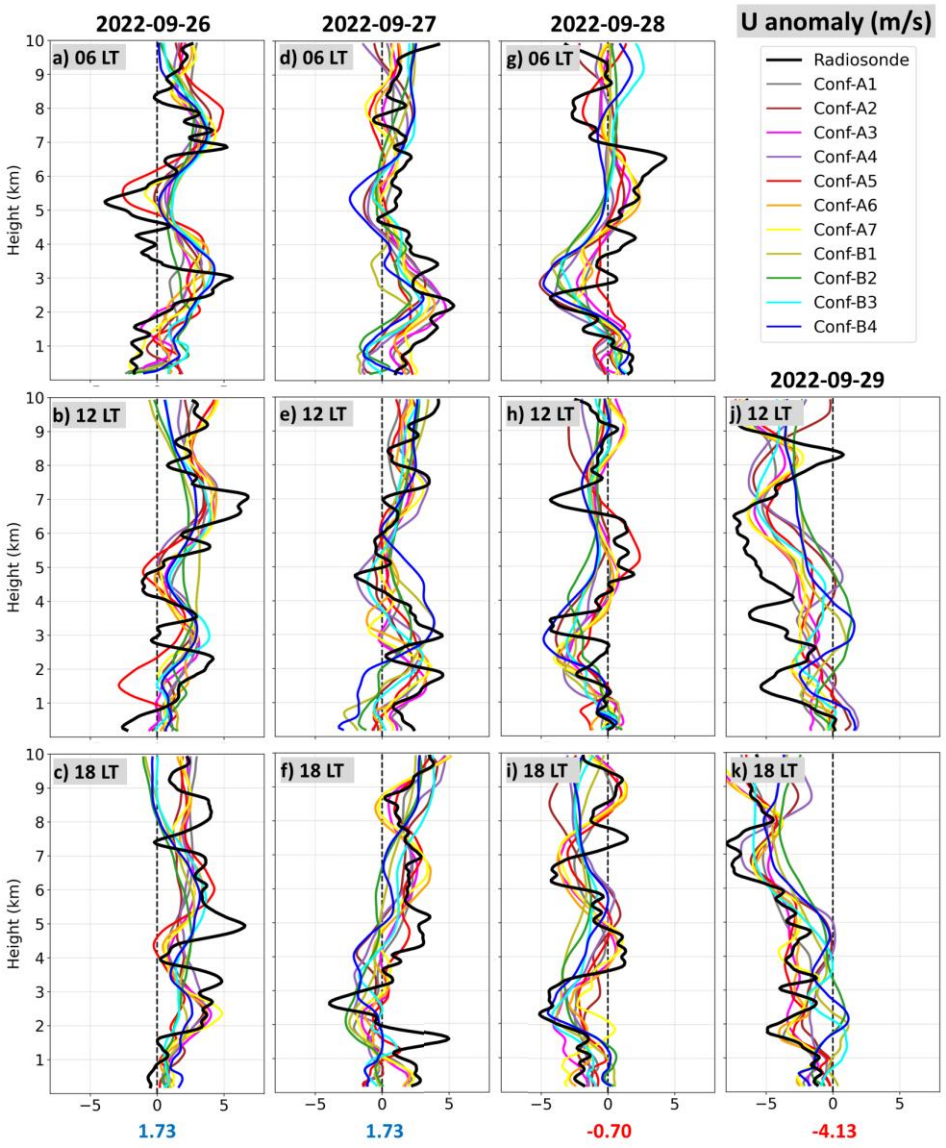

Figure 8. As in Fig. 5, but for U

Figure 9 shows the observed V anomalies (black lines) from 26 to 29 September 2022, illustrating a transition from positive to negative values. This shift reflects the MRG wave's progression from HP to LP systems, underscores its unique structure, and plays a vital role in generating the alternating patterns of convergence and divergence characteristic of these waves (Kiladis et al., 2009; Holton and Hakim, 2012). The observed reduction in positive anomalies to negative ones aligns with the established behavior of MRG waves.

The transition in V anomalies highlights how the MRG wave influences wind patterns not only in the zonal direction but also along the meridional axis. As the wave propagates, the negative V wind anomalies mark the trough where convergence is enhanced, supporting the upward motion and convective activity noted in earlier T and RH analyses (Kiladis et al., 2009).

Understanding the interplay between V and U winds is essential for capturing the full impact of MRG wave propagation on tropical atmospheric dynamics.

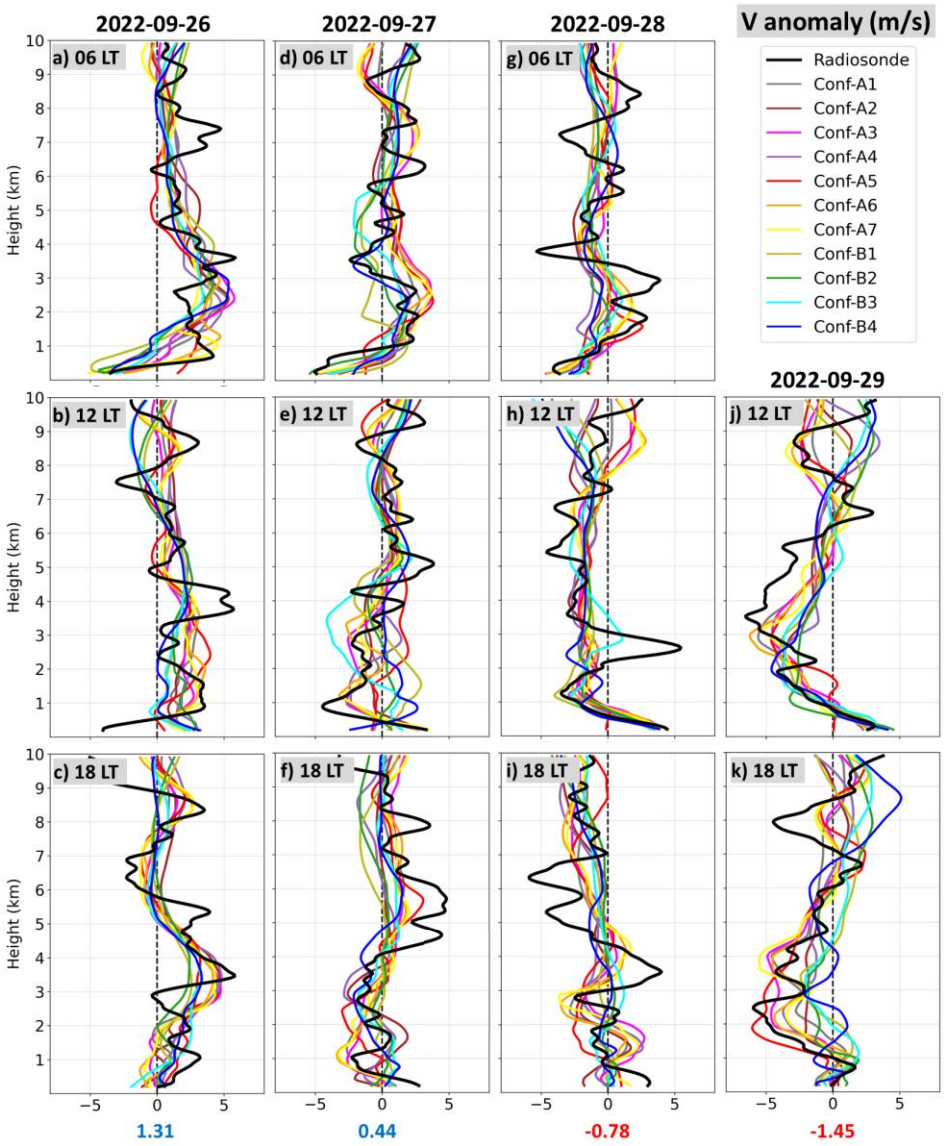

Figure 9. As in Fig. 5, but for V

Simulated V anomalies (colored lines) generally follow the observed trend, though with noticeable differences in variability across model configurations. The simulations often show less pronounced fluctuations than the radiosonde data, possibly because the model struggles to resolve the finer-scale processes influencing V wind fluctuations, such as sub-grid-scale turbulence. Discrepancies become more pronounced at higher altitudes (around 10 km on 28 and 29 September), where interactions with larger-scale circulations can amplify or distort the wave's meridional signature (Holton and Hakim, 2012). Consequently, while the WRF model captures lower and mid-tropospheric

MRG dynamics, it may be less accurate in depicting upper-level wind patterns.

In combination with analyses of U, P, T, and RH, these V anomalies provide a more comprehensive view of the MRG wave's impact on the tropical atmosphere. These combined wind signatures illustrate how MRG waves shape atmospheric circulation and drive changes in convection, moisture transport, and temperature (Kiladis et al., 2009; Holton and Hakim, 2012).

3.3. Analyses of R and NMAE

Figure 10 presents a set of Taylor diagrams that evaluate the performance of eleven WRF model configurations (A1, A2, A3, A4, A5, A6, A7, B1, B2, B3, B4) in simulating anomalies of P, T, RH, U, and V. For clarity, standard deviation and NMAE are scaled by factors of 35 and 30, respectively, divided by the maximum value across all datasets.

As shown in Fig. 10, among the meteorological variables analyzed, P attains the highest *R* (0.81), while RH presents the lowest *R* (0.21). In a related study, Sivaprasad et al. (2000) also found that WRF-simulated surface pressure yielded the highest *R* with buoy data during a tropical storm passage over the South China Sea (East Sea), which is consistent with the present findings. Furthermore, among all variables, the U wind exhibits the lowest NMAE (0.99), whereas temperature records the highest NMAE (1.41).

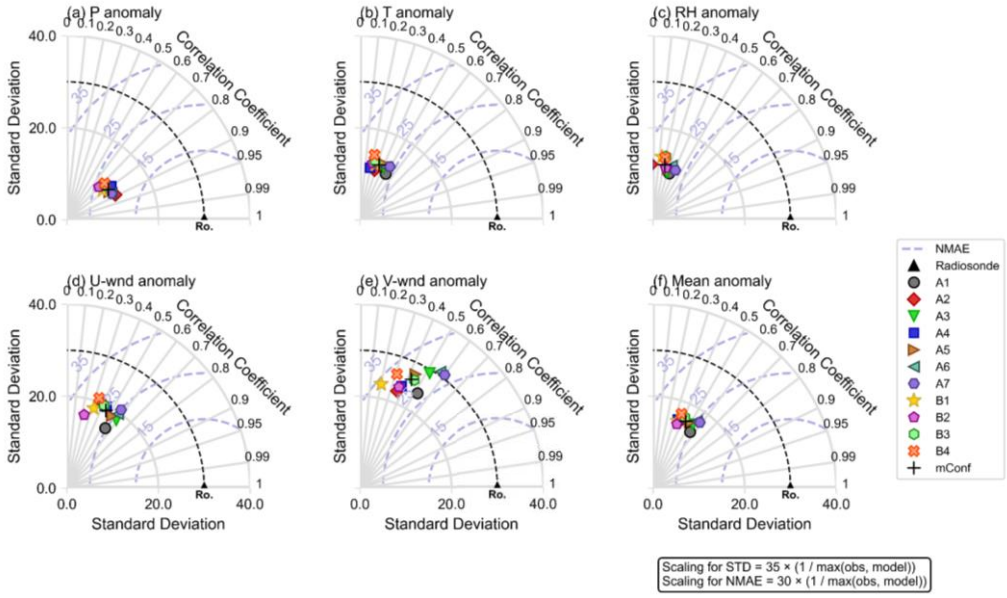

Figure 10. Taylor diagrams comparing 11 WRF configurations in simulating P, T, RH, U, V, and the mean anomalies. The angular axis shows R, the radial axis shows standard deviation, and dashed curves indicate NMAE. The dotted black arc represents radiosonde observations

Table 2 presents the results of significance tests comparing each WRF model configuration against radiosonde observations. The values represent the percentage of tests that show non-significant differences, indicating consistency between the model output and the observed data. Overall, all configurations exhibit excellent agreement with observations for P and T, with 100% non-significant results across the board. This suggests that the model reliably captures these two variables.

Among the tested configurations A1, A3, A5, A6, and A7, which use 2-step nesting

and FNL input consistently yield high percentages of non-significant differences across multiple variables. This suggests that these configurations perform particularly well at replicating observed atmospheric profiles and are more reliable at capturing the vertical structures of humidity and wind than other setups.

Table 2. Percentage of non-significant differences (%) from significance tests comparing each WRF model configuration (A1–A7, B1–B4) against radiosonde observations for P, T, RH, U, and V. The last row represents the mean across all configurations

Conf	Non-Significant difference (%)				
	P	**T**	**RH**	**U**	**V**
A1	100	100	55	64	82
A2	100	100	18	9	64
A3	100	100	55	55	73
A4	100	100	27	9	36
A5	100	100	45	64	36
A6	100	100	55	64	73
A7	100	100	55	64	73
B1	100	100	9	9	45
B2	100	100	18	9	36
B3	100	100	27	27	18
B4	100	100	18	9	27
Mean	**100**	**100**	**35**	**35**	**51**

Overall, configuration A7, corresponding to domain scheme A with FNL model input and 100 vertical levels, achieves the highest R (0.58) and the lowest NMAE (1.07). In general, configurations with domain scheme A (fewer nesting steps) with FNL input produce better results. The increased number of vertical levels appears to enhance *R* while reducing NMAE.

From Table 3, the configuration employing domain scheme A consistently demonstrates higher R and lower NMAE than domain scheme B. Increasing the number of vertical levels from 33 to 100 also yields higher *R* and lower NMAE, while using FNL model input yields superior performance relative to GFS input.

The dominant effect of model input is expected, as GFS supplies forecast-based atmospheric variables along with their uncertainties. In contrast, FNL provides the final analysis of atmospheric variables corrected by observations. Such differences highlight the chaotic nature of atmospheric dynamics, which limits the accuracy of weather prediction. In a related study, Talbot et al. (2012) also concluded that meteorological forcing data play the most critical role in shaping WRF model outcomes.

The difference between FNL- and GFS-driven simulations is notable. Using FNL analysis data in the WRF model increases the *R* with observed MRG-wave signals from 0.36 to 0.49 (36% relative improvement) and reduces the NMAE from 1.37 to 1.21 (12% decrease). This improvement highlights the importance of input data quality in accurately simulating MRG waves. FNL uses a multivariate data assimilation system that incorporates observations to produce consistent initial and boundary conditions. In contrast, GFS provides forecast data that may contain accumulated model biases and uncertainties, leading to lower *R* and higher NMAE in the nested domain.

Table 3. Sensitivity analysis of model performance based on domain scheme, vertical levels, and model input, using *R* and NMAE

	Domain		**Vertical Levels**					**Model Input**	
	Scheme A	Scheme B	33 Levels	45 Levels	60 Levels	80 Levels	100 Levels	FNL Input	GFS Input
R	**0.49**	0.36	0.40	0.41	0.49	0.55	**0.58**	**0.49**	0.36
NMAE	**1.21**	1.37	1.37	1.27	1.20	1.10	**1.07**	**1.21**	1.37

These results clearly show that tropical wave dynamics are susceptible to their forcing environment. Observations in the FNL data help guide the model toward a more

physically consistent solution. As demonstrated by Talbot et al. (2012), the choice of meteorological forcing can have a greater impact on WRF model performance than changes in physical parameterizations or grid resolution. For both research and operational forecasting, using high-quality input data is likely to improve model performance more than simply increasing resolution.

Regarding domain configurations, domain scheme A, which employs a simpler two-step nesting, outperforms the three-step nesting used in domain scheme B. Specifically, scheme A yields a higher R (approximately a 36% increase) and a lower error (around a 12% reduction). This improved performance may be attributed to the smaller outer domain in scheme A, which likely reduces boundary-induced errors, consistent with findings by Jee and Kim (2017). Furthermore, the additional nesting step in scheme B may introduce additional uncertainties due to increased complexity and potential error propagation.

Therefore, the better performance of domain scheme A compared to scheme B in simulating MRG wave structures is likely due to two main factors: error propagation at domain boundaries and complex interactions across different scales. First, using only two nests instead of three reduces the number of times data must be interpolated between parent and child domains. Each interpolation may introduce some error due to truncation and limited resolution. In a three-step nesting setup, these errors occur twice before reaching the innermost domain, potentially distorting the fine-scale features of MRG waves. The two-step setup reduces this error chain, helping to preserve the MRG waves' characteristics. Second, Scheme A has a smaller outer domain, which limits the area where large-scale circulation errors can influence the inner nest. In contrast, Scheme B's larger outer domain and additional nesting level may allow these spurious circulations to grow and interfere with the MRG signal, leading to unrealistic wave interactions in the innermost domain. In short, the two-step nesting creates a more straightforward, direct flow of information into the inner domain, resulting in a cleaner representation of equatorial MRG waves.

Most previous WRF studies (e.g., Jee and Kim, 2017) have used multi-step nesting mainly to balance model resolution with computing cost. However, few have directly compared two-step and three-step nesting in terms of their ability to simulate MRG waves accurately. This study finds that the simpler two-step nesting produces a higher R with observations, an essential result in tropical wave modeling. A key contribution of this study is that the two-step nesting not only reduces boundary error propagation but also achieves better agreement with observed MRG waves. This suggests that the nesting structure itself may play a critical role in determining model accuracy for synoptic-scale tropical wave dynamics.

Regarding vertical resolution, the sensitivity analysis shown in Table 3 highlights its strong influence on the WRF model's ability to simulate MRG waves. As the number of vertical levels increases from 33 to 100, the R improves consistently from 0.40 to 0.58, while the NMAE declines from 1.37 to 1.07. This trend indicates a significant enhancement in both phase accuracy and amplitude representation of the simulated MRG waves with finer vertical discretization.

Quantitatively, the increase of 18 points in R (from 0.40 to 0.58) corresponds to a 45% improvement in R strength. Similarly, the reduction in NMAE from 1.37 to 1.07 (0.30 points) reflects a 22% decrease in normalized error, suggesting that the simulations are both more accurate and more consistent with observations. These improvements are not marginal and emphasize

that vertical resolution is a major controlling factor for successfully resolving equatorial wave dynamics.

The underlying reason for this enhancement lies in the vertical structure and dynamics of MRG waves. A coarse vertical grid may fail to resolve key features such as the vertical phase tilt, the position of the critical level, or the detailed thermal and moisture structure within convective columns. In contrast, simulations with increased vertical levels can more accurately capture the fine-scale vertical gradients in temperature, humidity, and momentum, leading to better representation of baroclinic structures and wave-convection coupling.

Moreover, high vertical resolution enhances the model's ability to simulate wave-boundary layer interactions, cloud microphysics, and vertical moisture convergence, all of which are crucial to MRG wave maintenance and propagation. This is particularly important in the tropics, where the vertical stratification and latent heating profiles exert strong control on wave evolution. Therefore, the quantitative improvements in both R and NMAE confirm the benefits of a finer vertical resolution and highlight the necessity of sufficient vertical discretization when studying vertically structured phenomena such as MRG waves.

Figure 11 presents vertical profiles of RH, U, and V on 29 September 2022 at 18 LT, comparing radiosonde observations with WRF model simulations using domain scheme A, FNL input, and varying vertical resolutions (33, 45, 60, 80, and 100 levels). The figure reveals clear differences in model performance across vertical levels, particularly in the ability to resolve fine-scale vertical structures. Higher vertical resolution tends to improve the representation of vertical gradients and layered features. However, despite these improvements, none of the configurations fully replicate the detailed structures observed in the radiosonde data. This indicates that while increasing vertical resolution enhances simulation fidelity to some extent, limitations in model physics, resolution, or input data may still prevent the model from fully capturing the observed atmosphere's complexity.

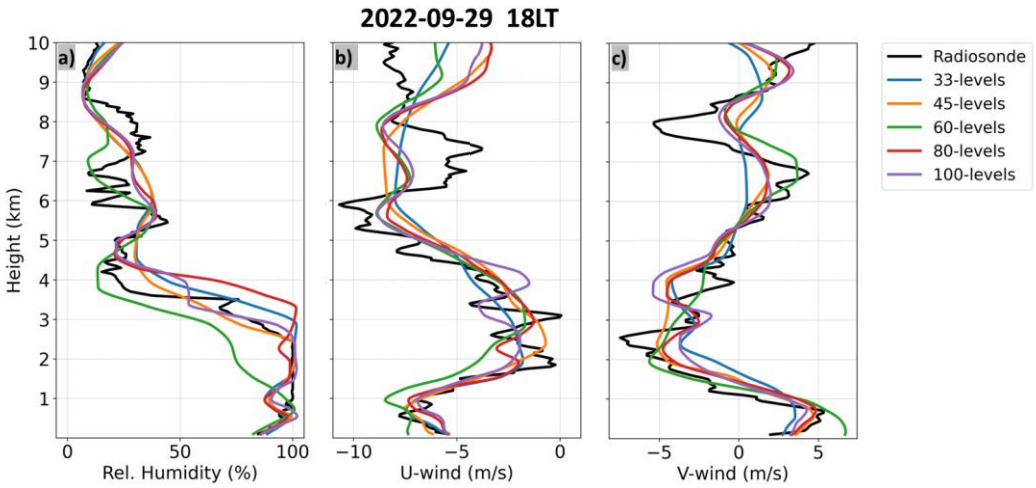

Figure 11. Vertical profiles of (a) RH, (b) U, and (c) V on 29 September 2022 at 18 LT, comparing radiosonde observations (black lines) with model simulations using 33, 45, 60, 80, and 100 vertical levels (colored lines). All configurations use two-step nesting and FNL input data

In the RH profiles (panel a), simulations with coarse vertical resolution (33 and 45 levels) fail to capture the sharp vertical gradients in the radiosonde data. Specifically, the sharp gradient between 3–4 km and the dry layer near 6–7 km is either smoothed out or not well-represented in these low-resolution runs. In contrast, finer-resolution simulations (60, 80, and 100 levels) demonstrate improved skill in resolving these features. Among them, the 80 and 100-level simulations closely follow the radiosonde, particularly in the mid-tropospheric moist and dry layers. However, the 60-level simulation underestimates RH above 4 km.

For U wind (panel b), the coarse-resolution runs underestimate the vertical structure of the easterly winds between 2 and 8 km. The vertical wind shear is poorly resolved, leading to overly smooth profiles. On the other hand, the 80- and 100-level runs reproduce both the magnitude and structure of the easterly winds and the vertical shear better. The 60-level simulation offers some improvement over the coarser setups but does not match the fidelity of the 80 and 100-level configurations.

In the V wind profile (panel c), the coarse-resolution runs again fail to capture detailed variations, which are important for representing vertical profiles. The 80- and 100-level simulations better match the radiosonde observations, especially in the upper troposphere.

Overall, the comparison highlights the importance of vertical resolution in capturing MRG wave-related structures. The coarse-resolution configurations (33 and 45 levels) are insufficient to resolve key features, such as sharp moisture gradients and wind shear layers, leading to oversimplified profiles. While increasing the number of vertical levels generally improves the simulation.

One of the primary reasons vertical resolution is essential is the model's ability to resolve the vertical phase structures associated with MRG waves. These waves often display distinct tilting of wind and temperature fields with height. Coarse vertical grids may fail to accurately capture these transitions, leading to errors in wave propagation and amplitude (Kiladis et al., 2009; Yang et al., 2007). Moreover, MRG waves play a critical role in modulating tropical convection, typically through interactions between wave dynamics and convective processes in the lower to mid-troposphere. High vertical resolution in these layers improves the simulation of such coupling, allowing for a more realistic representation of wave-convection feedbacks (Straub and Kiladis, 2003; Zhang, 2005).

Accurate vertical resolution is also crucial for representing the diabatic heating profiles associated with deep convection. These heating structures influence the development and propagation of equatorial waves, including MRG waves. If vertical levels are too sparsely distributed, the model may smear heating profiles across layers, weakening the dynamical response and disrupting the balance between wave and convective processes (Mapes, 2000). Additionally, MRG waves interact with low-level vertical shear and upper-tropospheric stability layers. Without sufficient resolution in these zones, particularly near the boundary layer top, the model may fail to capture essential instability mechanisms and vertical momentum transport.

Despite these benefits, improving vertical resolution comes with notable trade-offs and complexities. Increasing the number of vertical levels significantly increases computational cost due to smaller time steps required for numerical stability, higher memory usage, and larger output data volumes (Skamarock et al., 2008). This challenge is particularly acute when simulating gravity waves or other fast-propagating modes, as is the case with MRG waves. Furthermore, physical parameterizations, such as cumulus and boundary-layer schemes, are often tuned to

specific vertical grid configurations. Enhancing vertical resolution without recalibrating these schemes can introduce nonphysical behavior or cause model instability (Birner et al., 2006).

Another key challenge is the trade-off between vertical and horizontal resolution. Given limited computational resources, modelers must prioritize one over the other. For MRG waves, which span large horizontal scales (on the order of thousands of kilometers) but possess intricate vertical structures, it is sometimes more beneficial to focus on increasing vertical resolution, particularly in studies aimed at understanding wave dynamics rather than small-scale convection.

Vertical resolution is a critical factor in accurately simulating MRG waves. It enables the model to resolve key wave structures, capture convective interactions, and represent vertical shear and diabatic heating profiles more realistically. However, improving vertical resolution entails higher computational costs and may require adjustments to physical parameterizations. When balanced carefully, especially in the context of tropical wave modeling, high vertical resolution offers significant advantages and remains a recommended focus for improving simulation performance.

4. Conclusions

The numerical simulations of MRG waves along the southern coast of West Java using the WRF model have provided several important insights into model performance and the factors affecting MRG wave representation. By testing 11 configurations varying domain nesting (2 vs. 3-step nesting), vertical resolution (33, 45, 60, 80, and 100 levels), and input data (GFS vs. FNL) and comparing the results with radiosonde observations from Pameungpeuk Station during 26–29 September 2022, this study offers a detailed evaluation of how model setup influences simulation accuracy.

Overall, the simulations successfully captured the key atmospheric features of MRG wave propagation, including the modulation of pressure, temperature, relative humidity, and wind components, and effectively reflected the characteristic structure of MRG waves. However, a notable limitation emerged: the simulated vertical profiles exhibited reduced sensitivity and variability compared to the radiosonde data. This discrepancy, likely linked to lower vertical resolution, underscores the challenge of accurately modeling wave dynamics at fine scales.

Although none of the simulations fully capture the fidelity of the radiosonde observations, increasing the number of vertical levels markedly improves the WRF model's ability to simulate MRG waves. As the vertical resolution rises from 33 to 100 levels, the R improves by 45% and the NMAE decreases by 22%, indicating substantial gains in both phase accuracy and amplitude representation. These improvements highlight the critical role of vertical resolution in capturing the vertical structure and dynamics of equatorial waves.

Moreover, the domain's configuration proved influential. This study demonstrates that a simpler two-step nesting configuration (scheme A) outperforms the three-step setup (scheme B) in simulating equatorial MRG waves. Scheme A yields a higher R (36% increase) and lower error (12% reduction), likely due to reduced boundary error propagation and fewer interpolation steps. The smaller outer domain in scheme A may also limit the intrusion of large-scale circulation errors, resulting in a clearer representation of MRG wave structures. These findings highlight that nesting structure itself plays a critical role in accurately capturing tropical wave dynamics, and that a simpler two-step approach may offer a more effective and efficient solution for modeling MRG waves.

Additionally, this study also confirms that the quality of model input data plays a dominant role in accurately simulating MRG waves. Simulations driven by FNL analysis data, which incorporate observational corrections, show a significant improvement over those using GFS forecast data, raising the *R* with observed signals from 0.36 to 0.49 (a 36% increase) and reducing the NMAE by 12%. These results emphasize that tropical wave dynamics are susceptible to their forcing environment and that accurate initial and boundary conditions are essential for improving model fidelity. This study reinforces that the choice of meteorological forcing significantly impacts model performance, underscoring the importance of high-quality input data for both research and forecasting applications.

Although these results offer valuable insights into the performance of various WRF model configurations, they are derived from a single field campaign, limiting the scope and generalizability of the conclusions. A more comprehensive evaluation would require data from multiple campaigns encompassing a broader range of atmospheric conditions and MRG wave events, thereby enabling a more robust assessment of model performance and sensitivity.

Despite the limited dataset, the present findings serve as an essential preliminary step in evaluating the WRF model's ability to capture MRG wave dynamics. The observed correlations and errors provide constructive feedback on model configurations, particularly regarding model inputs, vertical resolution, and domain schemes. While these results must be interpreted cautiously due to the narrow database, they nonetheless offer a foundation for future optimization efforts and subsequent investigations with more extensive datasets.

In light of these findings, future research should focus on advanced data assimilation techniques to incorporate real-time observations more effectively and on expanding the range of case studies to enhance observational coverage. These steps will not only improve the simulation of MRG waves but also contribute to more reliable numerical weather prediction in tropical regions. Ultimately, this study lays a robust foundation for systematic enhancements in model physics, data assimilation, and domain configuration, deepening our understanding of MRG wave dynamics and advancing tropical weather forecasting.

Acknowledgements

We want to acknowledge the availability of the Weather Research and Forecasting (WRF) model, which has been instrumental in conducting this research. We thank the developers and the community behind the WRF model for their ongoing efforts to improve this valuable tool and for providing extensive support and documentation.

References

Aiyyer A.R., Molinari J., 2003. Evolution of mixed Rossby-gravity waves in idealized MJO environments. J. Atmos. Sci., 60, 2837–2855. Doi: 10.1175/1520-0469(2003)060%3C2837:EOMRWI%3E2.0.CO;2.

Andrews D.G., Holton J.R., Leovy C.B., 1987. Middle Atmosphere Dynamics, Elsevier, New York.

Argüeso D., Romero R., Homar V., 2020. Precipitation features of the maritime continent in parameterized and explicit convection models. J. Clim., 33, 2449–2466. Doi: 10.1175/JCLI-D-19-0416.1.

Barker D., Huang X.Y., Liu Z., Auligné T., Zhang X., Rugg S., Ajjaji R., Bourgeois A., Bray J., Chen Y., Demirtas M., Guo Y.R., Henderson T., Huang W., Lin H.C., Michalakes J., Rizvi S., Zhang X., 2012. The weather research and forecasting model's community variational/ensemble data assimilation system: WRFDA. Bulletin of the American Meteorological Society, 93(6), 831–843.

Bengtsson L., Dias J., Gehne M., Bechtold P., Whitaker J., Bao J.W., Magnusson L., Michelson S., Pegion P., Tulich S., Kiladis G.N., 2019. Convectively

coupled equatorial wave simulations using the ECMWF IFS and the NOAA GFS cumulus convection schemes in the NOAA GFS model. Mon. Weather. Rev., 147, 4005–4025. Doi: 10.1175/MWR-D-19-0195.1.

Birner T., Dörnbrack A., Schumann U., 2002. How sharp is the tropopause at midlatitudes? Geophysical Research Letters, 33(14). Doi: 10.1029/2002GL015142.

Chang C.-P., Harr P.A., Mcbride J., Hsu H.-H., 2004. Maritime continent monsoon: annual cycle and boreal winter variability. in: East Asian Monsoon, 107–150. Doi: 10.1142/9789812701411_0003.

Coniglio M.C., Correia J., Marsh P.T., Kong F., 2013. Verification of convection- allowing WRF model forecasts of the planetary boundary layer using sounding observations. Weather and Forecasting, 28(4), 842–862. Doi: 10.1175/WAF-D-12-00103.1.

Dias J., Gehne M., Kiladis G.N., Magnusson L., 2023. The role of convectively coupled equatorial waves in sub-seasonal predictions. Geophysical Research Letters, 50(21), e2023GL106198. Doi: 10.1029/2023GL106198.

Fathullah N.Z., Lubis S.W., Setiawan S., 2017. Characteristics of Kelvin waves and mixed Rossby-gravity waves in opposite QBO phases. IOP Conf. Ser. Earth Environ. Sci., 54. Doi: 10.1088/1755-1315/54/1/012032.

Feng Z., Leung L.R., Houze R.A.Jr., Hagos S., Hardin J., Yang Q., Han B., Fan J., 2018. Structure and evolution of mesoscale convective systems: Sensitivity to cloud microphysics in convection-permitting simulations over the United States. Journal of Advances in Modeling Earth Systems, 10(7), 1470–1494. Doi: 10.1029/2018MS001305.

Fonseca R.M., Zhang T., Yong K.T., 2015. Improved simulation of precipitation in the tropics using a modified BMJ scheme in the WRF model. Geosci. Model Dev., 8, 2915–1928. Doi: 10.5194/gmd-8-2915-2015.

Fritsch F.N., Carlson R.E., 1980. Monotone piecewise cubic interpolation. SIAM Journal on Numerical Analysis, 17(2), 238–246. Doi: 10.1137/0717021.

Geng B., Katsumata M., Taniguchi K., 2020. Modulation of the diurnal cycle of precipitation near the southwestern coast of Sumatra by mixed Rossby-gravity waves. J. Meteorol. Soc. Japan. Ser. II., 9. Doi: 10.2151/jmsj.2020-026.

Giannaros C., Melas D., Giannaros T.M., 2019. On the short-term simulation of heat waves in the Southeast Mediterranean: Sensitivity of the WRF model to various physics schemes. Atmospheric research, 218, 99–116. Doi: 10.1016/j.atmosres.2018.11.015.

Hernández K.S., Gómez-Ríos S., Henao J.J., Robledo V., Ramírez-Cardona A., Rendón A.M., 2024. Rainfall Sensitivity to Microphysics and Planetary Boundary Layer Parameterizations in Convection-Permitting Simulations over Northwestern South America. Journal of Meteorological Research, 38(4), 805– 825. Doi: 10.1007/s13351-024-3156-4.

Holton J.R., Hakim G.J., 2012. An introduction to dynamic meteorology: Fifth edition.

Hong S.Y., Lim J.O.J., 2006. The WRF single-moment 6-class microphysics scheme (WSM6). Asia-Pacific Journal of Atmospheric Sciences, 42(2), 129–151.

Im E.-S., Eltahir E.A.B., 2018. Simulation of the diurnal variation of rainfall over the western maritime continent using a regional climate model. Clim. Dyn., 51, 73–88. Doi: 10.1007/s00382-017-3907-3.

Jee J.-B., Kim S., 2017. Sensitivity study on high-resolution WRF precipitation forecast for a heavy rainfall event. Atmosphere (Basel), 8. Doi: 10.3390/atmos8060096.

Kiladis G.N., Dias J., Gehne M., 2016. The relationship between equatorial mixed Rossby–gravity and eastward inertio-gravity waves. Part I. J. Atmos. Sci., 73, 2123–2145. Doi: 10.1175/JAS-D-15-0230.1

Kiladis G.N., Wheeler M.C., Haertel P.T., Straub K.H., Roundy P.E., 2009. Convectively coupled equatorial waves. Rev. Geophys., 47. Doi: 10.1029/2008RG000266.

Koh T.Y., Wang S., Bhatt B.C., 2012. A diagnostic suite to assess NWP performance. Journal of Geophysical Research: Atmospheres, 117(D13). Doi: 10.1029/2011JD017103.

Lanzate J.R., Free M., 2008. Comparison of Radiosonde and GCM Vertical Temperature Trend Profiles: Effects of Dataset Choice and Data Homogenization. J. of Clim, 21, 5417–5435.

Lee H.-T., 2011. NOAA Climate Data Record (CDR). In: Of Daily Outgoing Longwave.

Liebmann B., Hendon H.H., 1990. Synoptic-scale disturbances near the equator. J. Atmos. Sci., 47, 1463–1479. Doi: 10.1175/1520-

0469(1990)047<1463:SSDNTE>2.0.CO;2.

Luers J.K., 1997. Temperature error of the Vaisala RS90 radiosonde. J. Atmos. Oceanic Technol., 14(6), 1520–1532. Doi: 10.1175/1520-0426(1997)014<1520:TEOTVR>2.0.CO;2.

Magana V., Yanai M., 1995. Mixed Rossby-gravity waves triggered by lateral forcing. Journal of Atmospheric Sciences, 52(9), 1473–1486. Doi: 10.1175/1520-0469(1995)052<1473:MRWTBL>2.0.CO;2.

Mapes B.E., 2000. Convective inhibition, subgrid-scale triggering energy, and stratiform instability in a toy tropical wave model. Journal of the Atmospheric Sciences, 57(10), 1515–1535. Doi: 10.1175/1520-0469(2000)057<1515:CISSTE>2.0.CO;2.

Marlyono S.G., Nandi N., 2018. The preparedness level of community in facing disaster in West Java Province. IOP Conf. Ser. Earth Environ. Sci., 145. Doi: 10.1088/1755-1315/145/1/012103.

Matsuno T., 1966. Quasi-geostrophic motions in the equatorial area. J. Meteorol. Soc. Japan. Ser. II., 44, 25–43. Doi: 10.2151/jmsj1965.44.1_25.

Mcbride J., 1998. Indonesia, Papua New Guinea, and tropical Australia: the southern hemisphere monsoon. Meteorol. Monogr, 89–99. Doi: 10.1007/978-1-935704- 10-2_3.

Minnis P., Yi Y., Huang J., Ayers K., 2005. Relationships between radiosonde and RUC-2 meteorological conditions and cloud occurrence determined from ARM data. J. of Geophy. Res., 110, D23. Doi: 10.1029/2005JD006005.

Nash J., Oakley T., Vömel H., Wei L., 2010. WMO intercomparison of high quality radiosonde systems. Tech. Rep., World Meteorological Organization, Yangjiang, China.

Neale R., Slingo J., 2003. The maritime continent and its role in the global climate: A GCM study. J. Clim., 16, 834–848. Doi: 10.1175/1520-0442(2003)016<0834:TMCAIR>2.0.CO;2.

Prihanto I.G., et al., 2023. Study on satellite disaster early warning system (SADEWA) acceptance with technology acceptance model. AIP Conference Proceedings, AIP Publishing, 2941, 1. Doi: 10.1063/5.0181481.

Qian J.-H., Robertson A.W., Moron V., 2010. Interactions among ENSO, the monsoon, and diurnal cycle in rainfall variability over Java, Indonesia. J. Atmos.Sci., 67, 3509–3524. Doi: 10.1175/2010JAS3348.1.

Radiation (OLR), Version 1.2. NOAA National Climatic Data Center. Doi: 10.7289/V5SJ1HH2.

Ramage C.S., 1968. Role of a "tropical maritime continent" in the atmospheric circulation. Mon. Weather. Rev., 96, 365–370. Doi: 10.1175/1520-0493(1968)096%3C0365:ROATMC%3E2.0.CO;2.

Ramos-Valle A.N., Prein A.F., Ge M., Wang D., Giangrande S.E., 2023. Grid spacing sensitivities of simulated mid-latitude and tropical mesoscale convective systems in the convective gray zone. Journal of Geophysical Research: Atmospheres, 128, e2022JD037043. Doi: 10.1029/2022JD037043.

Roundy P.E., Frank W.M., 2004. A climatology of waves in the equatorial region. Journal of the Atmospheric Sciences, 61(17), 2105–2132. Doi: 10.1175/1520-0469(2004)061<2105:ACOWIT>2.0.CO;2.

Satiadi D., Trismidianto, Purwaningsih A., Andarini D.F., Risyanto, Harjana T., Fathrio I., Praja A.S., Noersomadi, Nauval F., Saufina E., Juaeni I., Witono A., Nafiisyanti A., Harjupa W., Hermawan E., Muharsyah R.Y., Nuryanto D.E., 2024. Characteristics of atmospheric variables over the southern coast of West Java in the presence of Australian Monsoon and MRG waves. Kuwait. J. Sci., 51. Doi: 10.1016/j.kjs.2023.10.018.

Schreck C.J.III, Molinari J., Mohr K.I., 2011. Attributing tropical cyclogenesis to equatorial waves in the western North Pacific. Journal of the Atmospheric Sciences, 68(2), 195–209. Doi: 10.1175/2010JAS3396.1.

Sivaprasad P., et al., 2020. Simulation of the atmospheric parameters during passage of a tropical storm over the South China Sea (East Sea): a comparison with MetOcean buoy and ERA-Interim data. Meteorol. Appl., 27, e1895. Doi: 10.1002/met.1895.

Skamarock W.C., et al., 2021. A description of the advanced research WRF model version 4.3. Doi: 10.5065/1dfh-6p97.

Skamarock W.C., Klemp J.B., Dudhia J., Gill D.O., Barker D.M., Duda M.G., Huang X-Y., Wang W., Powers J.G., 2008: A description of the advanced research WRF version 3, NCAR Technical Note NCAR/TN–475+STR. National Center for Atmospheric Research.

Skamarock W.C., Klemp J.B., Dudhia J., Gill D.O., Barker D.M., Wang W., Powers J.G., 2019. A Description of the Advanced Research WRF Model Version 4. NCAR Technical Note.

Straub K.H., Kiladis G.N., 2003. Interactions between the boreal summer intraseasonal oscillation and higher-frequency tropical wave activity. Monthly Weather Review, 131(5), 945–960. Doi: 10.1175/1520-0493(2003)131<0945:IBTBSI>2.0.CO;2.

Straub K.H., Kiladis G.N., 2003. The observed structure of convectively coupled Kelvin waves: comparison with simple models of coupled wave instability. J. Atmos. Sci., 60, 655–1668. Doi: 10.1175/1520-0469(2003)060<1655:TOSOCC>2.0.CO;2.

Takasuka D., Satoh M., Yokoi S., 2019. Observational evidence of mixed Rossby- gravity waves as a driving force for the MJO convective initiation and propagation. Geophys. Res. Lett., 46, 5546–5555. Doi: 10.1029/2019GL083108.

Takayabu Y., 1994. Large-scale cloud disturbances associated with equatorial waves. J. Meteorol. Soc. Japan. Ser. II., 72, 433–449. Doi: 10.2151/jmsj1965.72.3_433.

Talbot C., Bou-Zeid E., Smith J., 2012. Nested mesoscale large-eddy simulations with WRF: performance in real test cases. J. Hydrometeorol., 13, 1421–1441. Doi: 10.1175/JHM-D-11-048.1.

Vömel H., Selkirk H., Miloshevich L., Valverde-Canossa J., Valdés J., Kyrö E., Kivi R., Stolz W., Peng G., J.A.Diaz, 2007. Radiation dry bias of the Vaisala RS92 humidity sensor. J. Atmos. Oceanic Technol., 24, 953–963. Doi: 10.1175/JTECH2019.1.

Wallace J.M., 1971. Spectral studies of tropospheric wave disturbances in the tropical western Pacific. Rev. Geophys., 9, 557–612. Doi: 10.1029/RG009i003p00557.

Wallace J.M., 1973. General circulation of the tropical lower stratosphere. Rev. Geophys., 11, 191–222. Doi: 10.1029/RG011i002p00191.

Wang L., et al., 2019. Convectively Coupled Equatorial Waves Simulated by CAMS-CSM. J. Meteorol Res, 33, 949–959. Doi: 10.1007/s13351-019-9021-1.

Wheeler M., Weickmann K.M., 2001. Real-time monitoring and prediction of modes of coherent synoptic to intraseasonal tropical variability. Monthly Weather Review, 129(11), 2677–2694. Doi: 10.1175/1520-0493(2001)129<2677:RTMAPO>2.0.CO;2.

Wheeler M.C., Kiladis G.N., 1999. Convectively coupled equatorial waves: analysis of clouds and temperature in the wavenumber-frequency domain. J. Atmos. Sci., 56, 374–399. Doi: 10.1175/1520-0469(1999)056<0374:CCEWAO>2.0.CO;2.

Wheeler M.C., Kiladis G.N., Webster P.J., 2000. Large-scale dynamical fields associated with convectively coupled equatorial waves. J. Atmos. Sci., 57, 613– 640. Doi: 10.1175/1520-0469(2000)057<0613:LSDFAW>2.0.CO;2.

Xalxo K.L., Mahala B.K., Mohanty P.K., Routray A., Mishra B.B., 2022. Performance assessment of WRF model radiation schemes in simulating the track and intensity of the super cyclonic storm "Amphan". Natural Hazards, 114(2), 1741–1762. Doi: 10.1007/s11069-022-05445-1.

Yanai M, Maruyama T., Nitta T., Hayashi Y., 1968. Power spectra of large-scale disturbances over the tropical Pacific. J. Meteorol. Soc. Japan., 46, 308–323. Doi: 10.2151/JMSJ1965.46.4_308.

Yanai M., Maruyama T., 1966. Stratospheric wave disturbances propagating over the equatorial Pacific. J. Meteorol. Soc. Japan. Ser. II., 44, 291–294. Doi: 10.2151/jmsj1965.44.5_291.

Yang G.-G., Slingo J., Hoskins B., 2009. Convectively coupled equatorial waves in high-resolution Hadley Centre climate Models. J. Clim., 22, 1897–1919. Doi: 10.1175/2008JCLI2630.1.

Yang G.-Y., Hoskins B.J., Slingo J.M., 2007. Convectively coupled equatorial waves. Part I: Horizontal and vertical structures. Journal of the Atmospheric Sciences, 64(6), 1560–1578. Doi: 10.1175/JAS4017.1.

Yu S., Eder B., Dennis R., Chu S.-H., Schwartz S.E., 2006. New unbiased symmetric metrics for evaluation of air quality models. Atmos. Sci. Lett., 7, 26–34. Doi: 10.1002/asl.125.

Zhang C., 2005. Madden-Julian Oscillation. Reviews of Geophysics, 43, RG2003. Doi: 10.1029/2004RG000158.